

# Basalt derived from highly refractory mantle sources during early Izu-Bonin-Mariana arc development

He Li (✉ [lihe@qdio.ac.cn](mailto:lihe@qdio.ac.cn))

Institute of Oceanology, Chinese Academy of Sciences <https://orcid.org/0000-0003-0363-0406>

**Richard Arculus**

Australian National University

**Osamu Ishizuka**

Geological Survey of Japan/AIST

**Rosemary Hickey-Vargas**

Florida International University

**Gene Yogodzinski**

Univ of South Carolina

**Anders McCarthy**

University of Bristol

**Yuki Kusano**

Geological Survey of Japan

**Philipp Brandl**

GEOMAR Helmholtz Centre for Ocean Research Kiel <https://orcid.org/0000-0001-6863-5262>

**Ivan Savov**

University of Leeds

**Frank Tepley III**

Oregon State University

**Wei-Dong Sun**

CAS Key Lab of Marine Geology and Environment, Center of Deep Sea Research, Institute of Oceanology, Chinese Academy of Sciences, Qingdao 266071 <https://orcid.org/0000-0002-9003-9608>

---

## Article

**Keywords:** basalt, subduction inception, island arc, Izu-Bonin

**Posted Date:** October 12th, 2020

**DOI:** <https://doi.org/10.21203/rs.3.rs-89845/v1>

**License:**  This work is licensed under a Creative Commons Attribution 4.0 International License.

[Read Full License](#)

---

1 **Basalt derived from highly refractory mantle sources during early Izu-**

2 **Bonin-Mariana arc development**

3 He Li<sup>1,2,3,4\*</sup>, Richard J. Arculus<sup>4,\*</sup>, Osamu Ishizuka<sup>5</sup>, Rosemary Hickey-Vargas<sup>6</sup>, Gene M.

4 Yogodzinski<sup>7</sup>, Anders McCarthy<sup>8</sup>, Yuki Kusano<sup>5</sup>, Philipp A. Brandl<sup>4,9</sup>, Ivan P. Savov<sup>10</sup>, Frank

5 J. Tepley III<sup>11</sup>, Weidong Sun<sup>1,2,3\*</sup>.

6  
7 1Center of Deep Sea Research, Institute of Oceanology, Chinese Academy of Sciences, Qingdao  
8 266071, China. <sup>2</sup>Laboratory for Marine Mineral Resources, Qingdao National Laboratory for Marine  
9 Science and Technology, Qingdao 266237, China. <sup>3</sup>Center for Ocean Mega-Science, Chinese Academy  
10 of Sciences, Qingdao 266071, China. <sup>4</sup>Research School of Earth Sciences, Australian National  
11 University, Canberra, ACT 2601, Australia. <sup>5</sup>Geological Survey of Japan/AIST, Central 7 1-1-1  
12 Higashi, Tsukuba, Ibaraki 305-8567, Japan. <sup>6</sup>Department of Earth & Environment, AHC5-394, Florida  
13 International University, Miami, FL 33199, USA. <sup>7</sup>Department of Earth & Ocean Sciences, University  
14 of South Carolina, Columbia, SC 29208, USA. <sup>8</sup>Institute of Earth Sciences, University of Lausanne,  
15 CH-1015 Lausanne, Switzerland, now at School of Earth Sciences, University of Bristol, Wills  
16 Memorial Building, Queens Road, Clifton BS8 1RJ, UK. <sup>9</sup>GEOMAR Helmholtz Centre for Ocean  
17 Research Kiel, Wischhofstrasse 1-3, 24148 Kiel, Germany. <sup>10</sup>School of Earth & Environment,  
18 University of Leeds, Leeds LS2 9JT, UK. <sup>11</sup>College of Earth, Ocean, and Atmospheric Sciences,  
19 Oregon State University, Corvallis, OR 97331, USA.

20

21

22 \*To whom correspondence should be addressed. E-mail: lihe@qdio.ac.cn,  
23 richard.arculus@anu.edu.au, weidongsun@qdio.ac.cn

24

25

26

27

28 **The character of magmatism associated with the early stages of subduction zone and**  
29 **island arc development is unlike that of mature systems, being dominated in the Izu-**  
30 **Bonin-Mariana (IBM) case by low-Ti-K tholeiitic basalts and boninites. Basalts**  
31 **recovered by coring the basement of the Amami Sankaku Basin (ASB), located west of**  
32 **the oldest remnant arc of the IBM system (Kyushu-Palau Ridge; KPR), were erupted at**  
33 **~49 Ma, about 3 million years after subduction inception. The chain of stratovolcanoes**  
34 **defined by the KPR is superimposed on this basement. The basalts were sourced from**  
35 **upper mantle similar to that tapped following subduction inception, and represented by**  
36 **forearc basalt (FAB) dated at ~52-51 Ma. The mantle sources of the ASB basalt basement**  
37 **were more depleted by prior melt extraction than those involved in the vast majority of**  
38 **mid-ocean ridge (MOR) basalt generation. The ASB basalts are low-Ti-K, aluminous**  
39 **spinel-olivine-plagioclase-clinopyroxene-bearing tholeiites. We show this primary**  
40 **mineralogy is collectively distinct compared to basalts of MOR, backarc basins of the**  
41 **Philippine Sea Plate, forearc, or mature island arcs. In combination with bulk**  
42 **compositional (major and trace element abundances plus radiogenic isotope**  
43 **characteristics) data for the ASB basalts, we infer the upper mantle involved was hot**  
44 **(~1400°C), reduced, and refractory peridotite. For a few million years following**  
45 **subduction initiation, a broad region of mantle upwelling accompanied by partial melting**  
46 **prevailed. The ASB basalts were transferred rapidly from moderate pressures (1-2 GPa),**  
47 **preserving a mineralogy established at sub-crustal conditions, and experienced little of**  
48 **recharge-mix-tap-fractionate regimes typical of MOR or mature arcs.**

49

50 **Keywords:** basalt | subduction inception | island arc | Izu-Bonin

51

52 Chains of explosive stratovolcanoes are characteristic of island and continental arcs such as the  
53 IBM and Andes respectively. These chains form a “volcanic front” typically no closer than 100  
54 km from the nearest trench, and lie ~105 km above the uppermost surface of a subducting  
55 lithospheric plate (“slab”)<sup>1,2</sup>. Basalt-dominated back-arc basins generated by seafloor spreading  
56 have formed during intervals in the history of most of the western Pacific arcs. These features  
57 have developed over several tens of millions of years. The trace element and isotopic  
58 characteristics of arc magmas are distinctive compared with the basalts of mid-ocean ridges  
59 (MORB) and those of isolated ocean islands (OIB) such as Hawaii. The distinctiveness derives  
60 from the fact that arc magmas have compositions modulated by involvement of slab-derived  
61 fluids and melts, and soluble trace elements entrained therein.

62 In a steady state, the pressure-temperature-dependent nature of the metamorphic mineral  
63 assemblages, and specifically hydrous phase stability that is established in the uppermost  
64 portion of a subducted slab, coupled with the thermal structure of the mantle wedge, control the  
65 depth at which slab-derived components are delivered to the wedge<sup>3,4</sup>. These factors impose  
66 the characteristic dimensions of volcanic front-trench-slab top distances identified above.  
67 However, subduction zones and arcs are ephemeral. Many of those currently active in the  
68 western Pacific were initiated about 50 Ma ago, possibly accompanying a major change in plate  
69 motions of the region<sup>5,6</sup>. The tectonic conditions preceding subduction inception have been  
70 hotly debated and attributed to spontaneous and induced modes<sup>7</sup>. The only active example of  
71 subduction inception is the Puysegur-Hjort system south of New Zealand<sup>8,9</sup>. Studies of the IBM  
72 system<sup>10,11</sup> and Central America<sup>12</sup> have however, established the broad tectonic and temporal  
73 framework in and during which the respective arcs were initiated. Prior to the establishment of  
74 a (quasi-)steady state in a given subduction zone system, the initial magmatic outputs in nascent  
75 arcs are of prime interest for their potential in revealing fundamental characteristics such as the  
76 nature of the earliest mantle wedge, temporal changes in the inputs from the subducted slab,

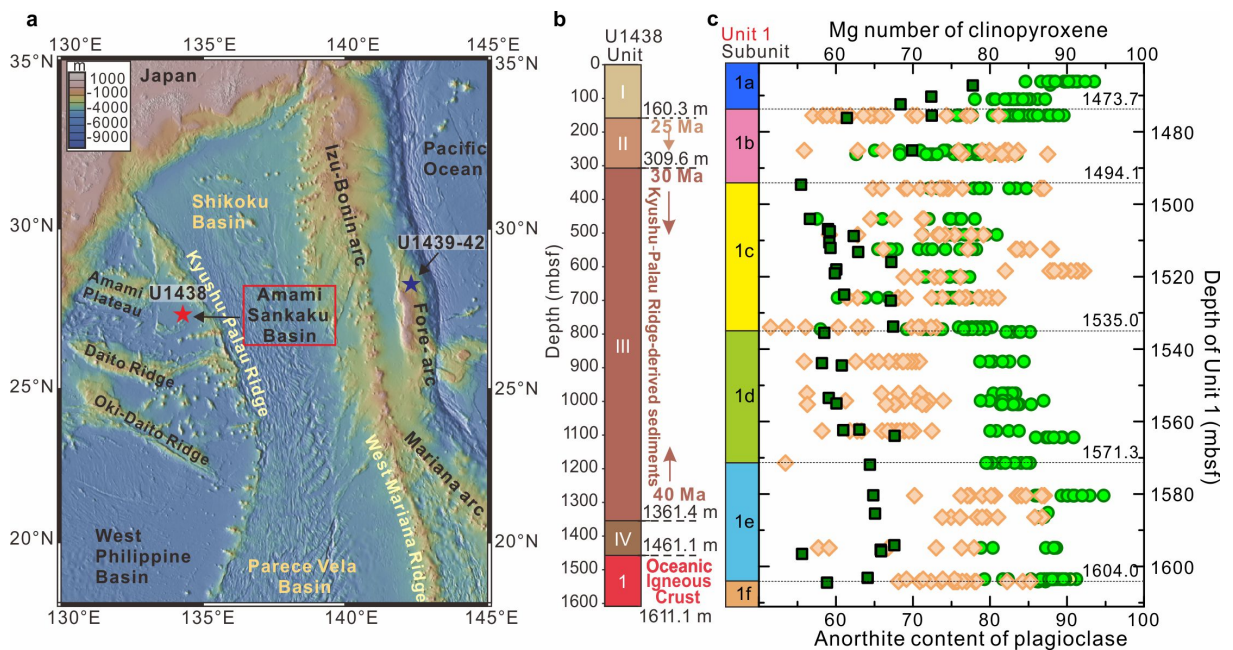
77 depths from which the magmas were derived, and petrological characteristics that serve to  
78 identify examples in the geological record.

79 Boninite magma (high-MgO; low-TiO<sub>2</sub>, intermediate SiO<sub>2</sub> (>8; <0.5; 53-63 wt%,  
80 respectively) sourced from a newly established mantle wedge together with FAB have been  
81 regarded as the archetypal nascent arc magma types<sup>10, 13, 14</sup>. Neither of these magma types are  
82 derived by partial melting of the slab. For example, hydrous partial melting of very hot,  
83 refractory (clinopyroxene-poor harzburgite) mantle sources at relatively low pressures (<2  
84 GPa) is indicated for boninite<sup>13,15</sup>.

85 The stratigraphy exposed both along the IBM trench wall and the western flank of the  
86 Ogasawara Ridge collectively reveals peridotite succeeded by gabbro, FAB and then boninite  
87<sup>10,14,16,17</sup>. Ages for FAB (and related gabbros) and boninite recovered at these locations by  
88 dredging, submersible and at International Ocean Discovery Program (IODP) Sites U1439 and  
89 U1442 (Figure 1), range from 51.9 to 51.3 Ma for FAB, and 51.3 to 50.3 Ma for boninite<sup>18</sup>.  
90 Boninite generation along the Ogasawara Ridge occurred between 48 and 45 Ma<sup>17, 19, 20</sup>.  
91 Younger (~45-44 Ma), boninite and 2-pyroxene andesites outcrop in the northern parts of the  
92 Chichijima Island group<sup>19</sup>. Tholeiitic basalts and andesitic (“calc-alkaline”) rocks 44-37 Ma  
93 age occur in the Hahajima islands, south of Chichijima<sup>20</sup>.

94 The Ti/V of both FAB and boninite is distinctly lower than MORB or the regional back-arc  
95 basin basalts (BABB), as a result of prior source mantle depletion in extractable melt, and  
96 perhaps of the higher oxidation state of the renewed partial melting process accompanying  
97 subduction inception<sup>14,21</sup>. The evidence for slab-derived trace element additions is equivocal in  
98 the basalts; enrichments in Rb and U relative to other potentially fluid-mobile and rare earth  
99 elements can be attributed to seafloor alteration in place rather than derived from the subducted  
100 slab.

101 In 2014, in addition to IODP expedition 352 to the forearc, expedition 351 explored the  
 102 foundations of the IBM system in the ASB (Site U1438) (Fig. 1a). Based on seismic evidence,  
 103 recovery was anticipated of the pre-IBM oceanic basement on which the earliest  
 104 topographically prominent arc, represented by the KPR chain of stratovolcanoes, is located.  
 105 However, beneath 1460 m of overlying sediments (Fig. 1b), the expedition penetrated 150 m  
 106 of basalt that shares much of the geochemical character<sup>22</sup> with but younger age (49 Ma)<sup>23</sup> than  
 107 FAB. The location of Site U1438, ~60 km southwest of the KPR, is a distal extreme from the  
 108 current trench of all IBM-related magmatism (Fig. 1). At the time of emplacement and  
 109 assuming no slab rollback, Site U1438 was at least 250 km distal from the position of the current  
 110 trench after accounting for subsequent backarc spreading in the Shikoku Basin and without  
 111 allowing for any subduction erosion along the trench<sup>24</sup>. The known distribution of low-Ti-K  
 112 tholeiitic basalts emplaced in the first few million years of the IBM arc system, is thus extensive,  
 113 both along- and across the strike of the arc<sup>16</sup>. Recognising this spatial and temporal distribution,  
 114 here we examine the most important petrological characteristics of the basalt comprising Unit  
 115 1 of ASB basalt (Fig. 1), and explore the distinctive conditions under which it was generated.



116

117 **Fig. 1. Location of IODP expeditions 351 (U1438) and 352 (U1439-42) drill sites, stratigraphy of U1438,**  
118 **bulk rock and mineral characteristics of Unit 1 at Site U1438.** a Bathymetric map<sup>25</sup> showing location of  
119 Amami-Sankaku Basin and Site U1438 adjacent to the Kyushu-Palau Ridge (remnant arc), and sites U1439-  
120 42 (Expedition 352) in the present-day fore-arc. b Unit thicknesses and ages at Site U1438. c subunit  
121 information for Unit 1 including Mg number ( $100 \cdot \text{Mg}/(\text{Mg} + \text{Fe}^{2+})$ ) of clinopyroxene (green circles), anorthite  
122 content (An%) of plagioclase (orange diamonds), and bulk rock  $100 \cdot \text{Mg}/(\text{Mg} + \Sigma \text{Fe})$  (dark green squares)  
123 versus depth.

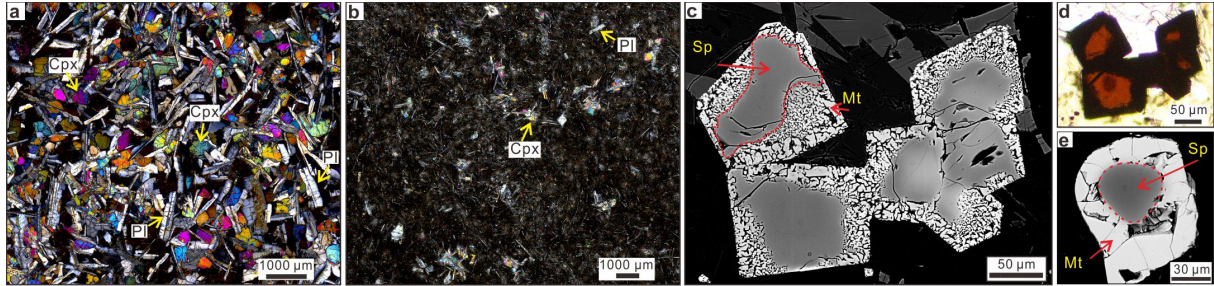
124

## 125 **Results**

### 126 **Petrology of Unit 1 ASB basalt**

127 On the basis of morphology, chemical composition, and isotopic characteristics, the basalt sheet  
128 lavas and pillows comprising Unit 1 have been divided into several subunits (a to f; Fig. 1c)<sup>26</sup>.  
129 <sup>27</sup>. Representative examples in thin-section of the textures and minerals of the subunits are  
130 shown in Fig. 2 and Supplementary Fig. 1. Textures range from glassy through fine-grained  
131 microcrystalline to medium-grained, phyrlic to sparsely microphyric, plus some that are  
132 intersertal to medium-grained sub-ophitic. The phenocryst and microphenocryst mineralogy  
133 comprises plagioclase, clinopyroxene, olivine and spinel. Based on the petrographic  
134 relationships and trace element variations in the respective minerals, a crystallisation order of  
135 spinel, olivine, plagioclase, and clinopyroxene is inferred. All minerals appear fresh except for  
136 olivine, which is mostly pseudomorphed by chlorite and calcite. Some olivine in subunit 1b has  
137 a composition of Fo<sub>90-90.5</sub>, which is considerably more Mg-rich than the clinopyroxene (Mg  
138 number 80-75) of the same subunit. The groundmasses vary from glassy (average 35% and <  
139 85%) to holocrystalline comprising plagioclase, clinopyroxene, and magnetite. One section is  
140 moderately vesiculated (30%) but the majority are sparsely to non-vesicular. Many flow  
141 contacts exist, some with (altered) glassy margins but most with gradational changes in grain  
142 size. Numerous thin (<3mm) and branching veins filled with calcite, chlorite, and clay minerals

143 are present throughout Unit 1. Logging shows zones of varying redox where the veins also  
144 contain either hematite, or pyrite, or magnetite; other sections have blotches and veins of  
145 chlorite<sup>26</sup>.

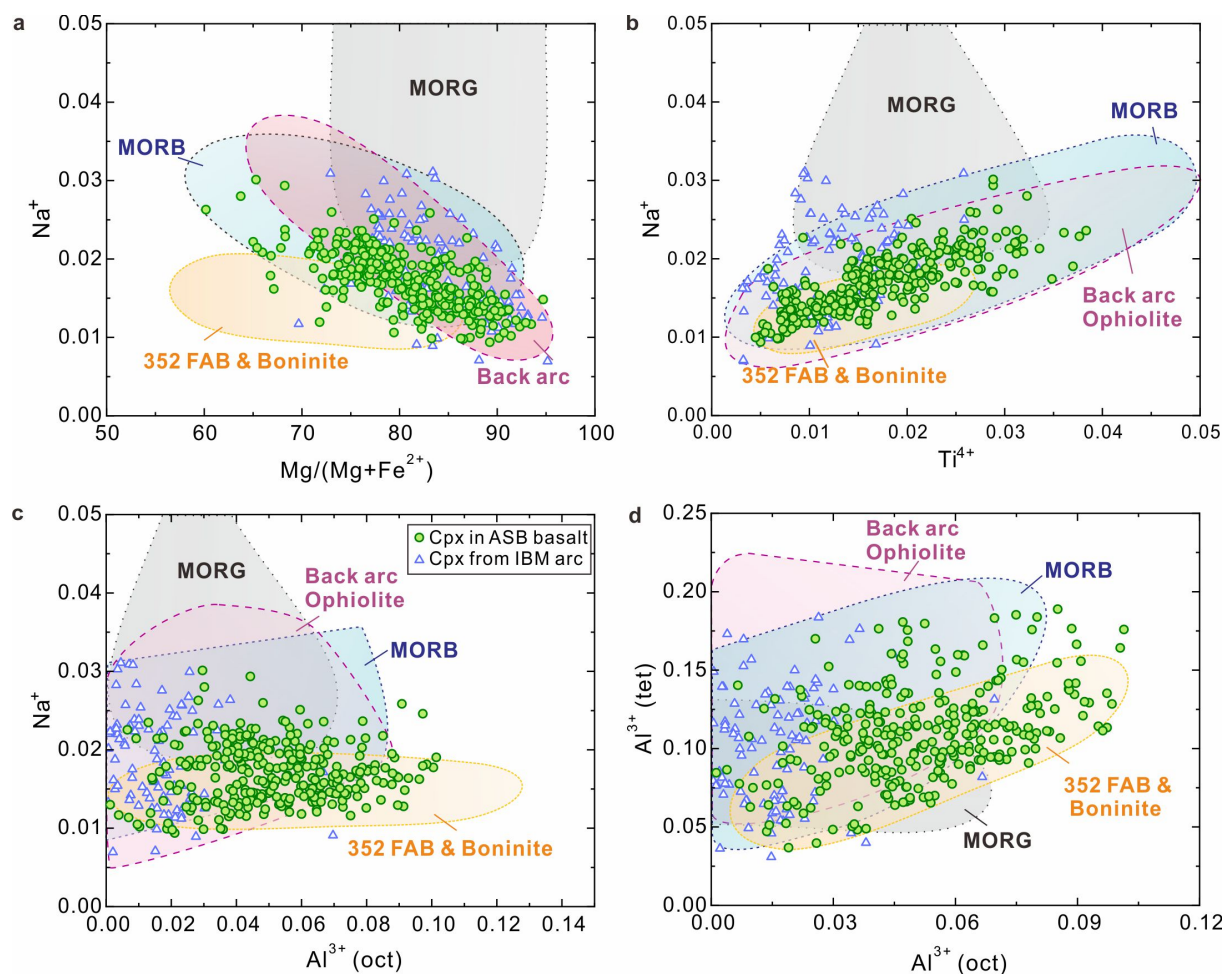


146  
147 **Fig. 2. General and detailed photomicrographs of Unit 1 ASB basalts.** a Medium-grained basalt from  
148 subunit 1c (78R3 21-25), including clinopyroxene (Cpx) and plagioclase (Pl) crystals (crossed polars). b  
149 Fine-grained basalt (84R1 84-87) from subunit 1e, with small crystals of clinopyroxene and plagioclase  
150 (crossed polars). c Back-scatter electron images of spinel; darker color within the red dash line is aluminous  
151 spinel; brighter color outside the red dash line is symplectitic magnetite. d Transmitted light image of the  
152 same spinel shown in c, red color is the Al-rich cores, and opaque boundaries are magnetite. e Back-scatter  
153 image of spinel, Al-rich core surrounded by magnetite-rich rim outside the red dash line.

154  
155 The MgO contents of Unit 1 ASB basalt varies from 13.8 to 6.7 wt% with a mean of 8.6  
156 wt%; highest values are in subunits 1a and e<sup>26</sup>. The higher values of subunit 1a may be affected  
157 by seawater alteration, given elevated Na, K and soluble trace element (Rb, U) abundance  
158 characteristics<sup>26</sup>. However, the persistent offset and tracking of the Mg number  
159 ( $100 \cdot \text{Mg}/(\text{Mg} + \text{Fe}^{2+})$ ) of the clinopyroxene at higher values than those of the host rock  
160  $100 \cdot \text{Mg}/(\text{Mg} + \Sigma \text{Fe})$  shown in Figure 1c for all subunits, is consistent with intrinsically high  
161 MgO contents of Unit 1 basalts compared with MORB (mean 7.58 wt%; generally < 10 wt%)<sup>28</sup>.  
162 The high Cr ( $\leq 500$  ppm) and Ni ( $\leq 350$  ppm) of Unit 1 lavas are also consistent with a primitive  
163 character. The TiO<sub>2</sub> contents range from 0.6 to 1.2 wt. % with a mean of 0.9; this is significantly  
164 lower than that of MORB (mean = 1.68 wt%)<sup>28</sup>. Some lavas of the high Mg# subunit 1e have  
165 K<sub>2</sub>O contents < 0.02 wt%<sup>23</sup>, which is an order of magnitude less than the mean for MORB (0.16

166 wt%<sup>28</sup>). The majority of the lava of Unit 1 can accordingly be classified as low-Ti-K tholeiitic  
167 basalts on the basis of their low-Ti-K in combination with total alkalis vs. silica contents<sup>29</sup>.

168 The presence of (micro)phenocrystic clinopyroxene (Fig. 2) in all Unit 1 ASB basalts is  
169 remarkable compared with the typical truancy of this phase as a phenocryst in primitive [high  
170  $100 \cdot \text{Mg}/(\text{Mg} + \Sigma\text{Fe})$ ] MORB<sup>30</sup>. Clinopyroxene is unequivocally involved in the establishment  
171 of the overall major and trace element variation patterns in the global MORB compositional  
172 array<sup>31</sup>, and is a major component of gabbros recovered from MOR sections (e.g., <sup>32</sup>). The  
173 clinopyroxene in Unit 1 basalts spans a range from diopside to augite according to the IMA  
174 classification<sup>33</sup>, with Mg numbers up to 95 (Figs. 1c, 3a). Major and trace element analyses are  
175 presented in Supplementary Table 1, and additional major elements only in Supplementary  
176 Table 2. Selected grouped binary compositional plots of these analyses are presented in Fig. 3.  
177 Data for clinopyroxene in individual subunits and Unit III<sup>35</sup> are shown in Supplementary Fig.  
178 2. Unit III comprises volcanoclastic-rich sediments of Eocene-Oligocene-age derived from the  
179 KPR<sup>35</sup> (data in Supplementary Table 3). In Figure 3, comparative data are displayed for:  
180 clinopyroxene grains from within the oldest sediments recording nascent IBM arc (Unit IV;  
181 Eocene age<sup>34</sup>) overlying Unit 1 ASB basalt; mid-ocean ridge basalts and gabbros (MORB/G;  
182 references in Supplementary Material); 352 FAB and boninite<sup>36</sup>, Oman ophiolite<sup>37</sup> and backarc  
183 basalts (Data from PetDatabase website) (Fig. 3, Supplementary Figure S2).



184

185 **Fig. 3. Clinopyroxene compositions in 351 Unit 1 of ASB basalt compared with 351 Unit IV**  
 186 **recording the nascent IBM arc<sup>34</sup> just above the ASB basalt, mid-ocean ridge basalt and gabbro**  
 187 **(MORB/G), 352 FAB and boninite<sup>36</sup>, Oman ophiolite<sup>37</sup> and backarcs (Data from PetDatabase website).**

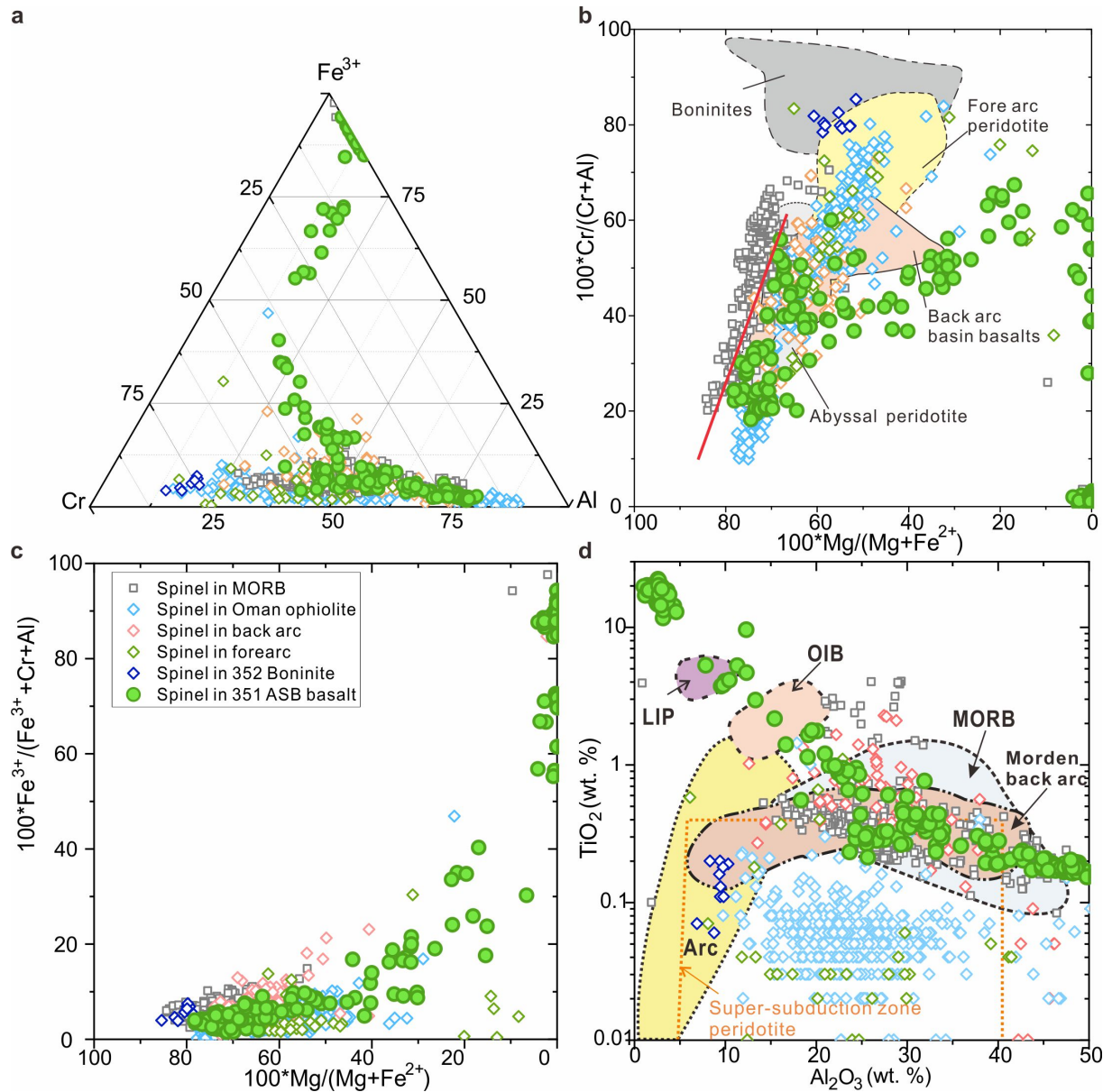
188 a  $\text{Na}^+$  versus  $100 \cdot \text{Mg}/(\text{Mg} + \text{Fe}^{2+})$  for clinopyroxene in Unit 1 ASB basalt and Unit IV recording the nascent  
 189 IBM arc<sup>34</sup>, showing compositional overlap compared with clinopyroxene in MORB/G and backarcs, but a  
 190 contrasted trend compared with FAB and boninite; b.  $\text{Na}^+$  versus  $\text{Ti}^{4+}$ . c  $\text{Na}^+$  versus octahedrally-coordinated  
 191  $\text{Al}^{3+}$ . d Tetrahedrally-coordinated versus octahedrally-coordinated  $\text{Al}^{3+}$  ( $\text{Al}^{3+}$  (tet) and  $\text{Al}^{3+}$  (oct) respectively).  
 192 All cations calculated on the basis of 6 oxygen anions. References for data sources used for clinopyroxene  
 193 in MORB/G are in the Supplementary Material.

194

195 Some features of the comparative clinopyroxene compositional plots are clear: 1. Na is  
 196 negatively correlated with Mg number, and positively correlated with Ti in both unit 1, III, and  
 197 IV (Figs. 3a, b, S2); 2. Na is much lower at high Mg number than those in MORB/G. (Fig. 3a);

198 3. Unit 1 clinopyroxene is generally distinctly more aluminous in both tetrahedrally- and  
199 octahedrally-coordinated Al than in clinopyroxene of Unit III or IV and extends to more  
200 aluminous compositions than MORB/G. Subunits a and e have the highest Mg number  
201 decreasing through f and d to subunits b and c. In contrast, clinopyroxene for all subunits spans  
202 a similar range of Al (tetrahedrally- and octahedrally-coordinated).

203 The spinel in Unit 1 basalts is compositionally unusual on a global comparative basis<sup>38, 39</sup>  
204 Analyses are presented in Supplementary Table 4, and some representative photomicrographs  
205 are displayed in Fig. 2 (c-e). Grouped ternary and binary spinel compositional plots are shown  
206 in Fig. 4. Overall, the spinel in Unit 1 basalts has a unique compositional range compared  
207 with spinel in the most abundant basalt types of MOR, arcs, ocean islands and their possible  
208 progenitors, the large igneous provinces. Compositions form a continuum extending from Al-  
209 Cr-rich (pleonaste-chromite) to Ti-Fe<sup>3+</sup>-rich (titaniferous magnetite).



210

211 Fig. 4. Spinel compositions in 351 Unit 1 ASB basalt compared with mid-ocean ridge basalts (MORB)<sup>38</sup>,

212 <sup>40</sup>, 352 boninite<sup>36</sup>, forearc, backarc and Oman ophiolite (data from PetDatabase website) **a** Cr-Al-Fe<sup>3+</sup>

213 diagram. **b** 100\*Cr/(Cr+Al) versus 100\*Mg/(Mg+Fe<sup>2+</sup>). **c** 100\*Fe<sup>3+</sup>/(Fe<sup>3+</sup>+Cr+Al)) versus

214 100\*Mg/(Mg+Fe<sup>2+</sup>). **d** TiO<sub>2</sub> (wt. %) versus Al<sub>2</sub>O<sub>3</sub> (wt.%). Green solid circles are spinel in unit 1 and gray

215 solid square symbols are spinel in MORB. Red line in **b** delimits the highest Mg/(Mg+Fe<sup>2+</sup>) for a given

216 Cr/(Cr+Al) of the abyssal harzburgite array<sup>41</sup>. Other abbreviations are: OIB = ocean island basalt; LIP =

217 large igneous province.

218

219 In the Al-Cr-rich range, Unit 1 spinel extend to more aluminous compositions than those of  
220 MORB<sup>38, 40</sup> (Fig. 4a), but have slightly lower Mg numbers (Fig. 4b, c). A notable feature is  
221 the Unit 1 spinel are consistently offset to lower Mg number for a given Cr/(Cr+Al) (Fig. 4b)  
222 and lower Fe<sup>3+</sup>/(Cr+Al+Fe<sup>3+</sup>) (Fig. 1c) than spinel in MORB. Both features are consistent  
223 with derivation from refractory peridotite sources and more reduced host magmas in the case  
224 of ASB basalt than for MORB<sup>41, 42</sup>. In detail, the patterns of compositional zonation are  
225 complex, with spinel in the more evolved (lower Mg number) subunits b and c showing the  
226 most extensive and continuous zonation patterns (Supplementary Fig. 3). The general trend is  
227 characterised by relatively Al-rich cores zoned outwards through Cr- to Fe<sup>3+</sup>-rich  
228 compositions (Supplementary Fig. 4). Highly aluminous-spinels with the highest Al<sub>2</sub>O<sub>3</sub>  
229 content (47 wt. %) in Unit 1 have the highest MgO contents (19.6 wt.%); these are higher  
230 than those in the majority of MORB, i.e. basaltic glasses from the Mid-Atlantic Ridge <sup>40</sup>.

231 Plagioclase is generally the most abundant mineral phase in Unit 1 ASB basalts. Analyses  
232 are presented in Supplementary Data Table 5. The range of compositions differs by subunit  
233 (Fig. 1c). In dry basalt magmas such as MORB, there is generally a consistent relationship  
234 between the forsterite contents of olivine with the anorthite contents of plagioclase (e.g., Fo<sub>90</sub>  
235 in equilibrium with An<sub>80</sub>)<sup>43</sup>. In the case of comparatively wet arc basalts however, this  
236 correspondence is decoupled with the coexistence of markedly anorthitic plagioclase in  
237 equilibrium with less forsteritic olivine<sup>44, 45</sup>. The Mg number of clinopyroxene in equilibrium  
238 with plagioclase mimics that of olivine. With the exclusion of subunit 1a wherein the  
239 plagioclase is a quench phase in the groundmass, the ranges in plagioclase composition are: b,  
240 An<sub>88-52</sub>; c, An<sub>92-52</sub>; d, An<sub>74-56</sub>; e, An<sub>87-54</sub>; f, An<sub>85-68</sub>. The decoupling of clinopyroxene Mg  
241 numbers and anorthite content of plagioclase is manifest in Fig. 1c. For example, the Mg  
242 numbers of clinopyroxene in Subunit 1d are consistently higher than the anorthite contents of  
243 the plagioclase; in contrast, much of the plagioclase in Subunit 1c is considerably more calcic

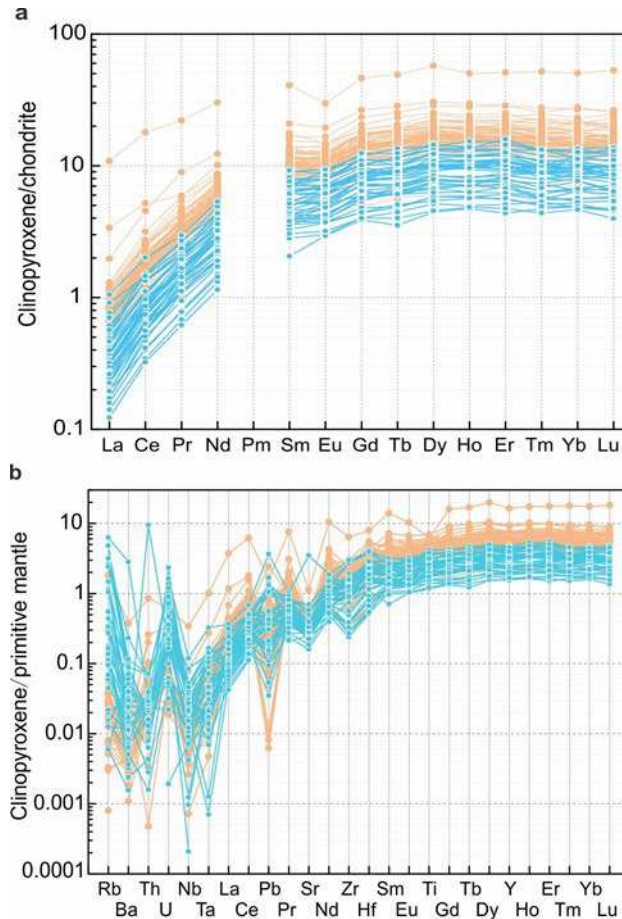
244 than that of Subunit 1d, and considerably exceeds in numerical value the Mg number of the  
245 coexisting clinopyroxene. This type of pattern can be interpreted to reflect a wetter, evolved  
246 character (low  $Mg/(Mg + \Sigma Fe)$ ) of the host magma of 1c in contrast to the similarly evolved but  
247 relatively dry host of 1d. The fine-grained texture of 1d contrasts with the generally more phyrlic  
248 nature of 1c (Supplementary Fig. 1), and likely reflects the relative dissolved water contents of  
249 the host subunit magmas.

250

### 251 **Trace elements of clinopyroxene**

252 The trace element abundances of clinopyroxene are critically important for assessing the  
253 pristinity of the bulk trace element abundances of the Unit 1 ASB basalts. The partitioning of  
254 many trace elements, particularly the rare earths for example between clinopyroxene and basalt  
255 magma, is systematic and well understood<sup>46</sup>. Given the evidence for some seawater alteration  
256 of portions of the Unit 1 ASB basalts, the trace element abundances of the apparently pristine,  
257 unaltered clinopyroxene serves as an important monitor of the original trace element  
258 characteristics of the host magmas. The trace element abundances are presented in  
259 Supplementary Table 1. Chondrite-normalised rare earth element (REE) and primitive mantle-  
260 normalised<sup>47</sup> multi-element plots for representative high- and low-  $Mg/(Mg + \Sigma Fe)$  subunits (e  
261 and c, respectively) are shown in Fig. 5. The general coupled variation of the  $Mg/(Mg + \Sigma Fe)$  of  
262 the host basalt with Mg number of the clinopyroxene shown in Fig. 1c is sustained in the  
263 systematics of REE abundances. There is some overlap between clinopyroxene in subunits e  
264 and c (bulk rock high- and low- $Mg/(Mg + \Sigma Fe)$  respectively), but the abundances of all the REE  
265 in subunit 1e range to much lower values (e.g., La at 0.1\* chondritic) than those of 1c, which  
266 conversely extend to much higher values (La at 10\* chondritic) of all the REE. The order-of-  
267 magnitude range in abundances of a given rare earth for clinopyroxene in a specific subunit  
268 might relate to open system behaviour of magma reservoirs tapped during eruption of Unit 1

269 basalts<sup>48</sup>. The trace element abundances of clinopyroxene in the other subunits are displayed in  
 270 Supplementary Fig. 5; similar relationships between  $Mg/(Mg+\Sigma Fe)$  of the subunit whole-rocks  
 271 and the degrees of enrichment of the REE exist.



272  
 273 **Fig. 5.** Trace element abundances for clinopyroxene. **a** Chondrite-normalized<sup>47</sup> rare earth element  
 274 abundances for clinopyroxene in subunits 1c and 1e of ASB basalts. **b** Primitive mantle-normalized<sup>47</sup> trace  
 275 element abundances for clinopyroxene in subunits 1c and 1e. Yellow circles are data for subunit 1c and blue-  
 276 green circles for subunit 1e.

277  
 278 The crystallization order of plagioclase and clinopyroxene is related to the H<sub>2</sub>O content of  
 279 the host melt<sup>49</sup>. Petrographic evidence can be ambiguous. Plagioclase has a greater preference  
 280 for Eu<sup>2+</sup> than clinopyroxene and the presence or otherwise of negative Eu anomalies in  
 281 clinopyroxene is an indicator of prior plagioclase fractionation from a specific magma host.  
 282 The overall range of Eu anomalies calculated using measured chondrite-normalised abundances

283 of the specific elements in  $\text{Eu}/\sqrt{(\text{Sm}*\text{Gd})}$ , is 1.2 to 0.6, with a mean value of expected/measured  
284  $\text{Eu} = 0.88 (\pm 0.09)$ . Even the clinopyroxene with the highest Mg numbers in the most primitive  
285 subunits have this level of negative Eu anomaly; accordingly we infer saturation with  
286 plagioclase prior to clinopyroxene in all subunits of Unit 1.

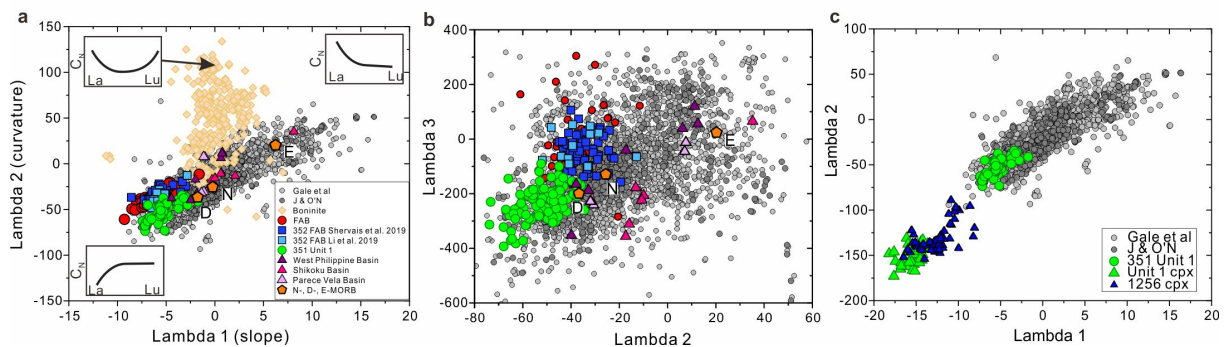
287 The high abundances of potentially fluid-mobile trace elements (e.g., alkalis, alkaline earths,  
288 Pb and U) relative to immobile elements such as Nb and Zr, are a distinctive feature of arc  
289 magmas relative to MORB and OIB<sup>50</sup>. While none of these elements are strongly partitioned  
290 into clinopyroxene relative to coexisting melt, their abundances are nevertheless systematically  
291 related to those of a melt by the respective partition coefficients<sup>46</sup>. The primitive mantle-  
292 normalised abundances of these elements together with the REE in clinopyroxene of subunits  
293 e and c, have some distinctive characteristics: Rb and U are predominantly enriched relative to  
294 Nb, but Ba and Th are not (Fig. 5b). This decoupling is unusual. The abundance of Pb relative  
295 to Ce (nominally an element of similar peridotite-melt partitioning behaviour) is highly variable  
296 while Sr is generally depleted relative to Nd. These characteristics are typical of all  
297 clinopyroxene in Unit 1 (Supplementary Fig. 5). One interpretation of the decoupling is that Rb  
298 and U are elements typically enriched by circulation and reaction of seawater with basalts on  
299 the seafloor, whereas Th is not<sup>51</sup>. Elevated Unit 1 bulk-rock  $^{87}\text{Sr}/^{86}\text{Sr}$  (0.7033-0.7060)<sup>52</sup> is  
300 consistent with such a process. However, these patterns are present in apparently pristine  
301 clinopyroxene crystals with no signs of alteration.

302

### 303 **Trace element comparisons**

304 The systematic geochemical behaviour of the REE is of prime importance for understanding  
305 the processes of partial melting of the mantle, and fractional crystallisation of the resultant  
306 magmas. Quantification of the shapes of chondrite-normalised REE abundance patterns<sup>53</sup> is  
307 particularly useful for systematically comparing the global array of ocean floor basalts with

308 those of Unit 1 and FAB. In Figure 6, the slope (lambda1), curvature (lambda 2), and extent of  
 309 sigmoidal character (lambda 3) of respective patterns are displayed. The important features are  
 310 Unit 1 basalts have the among most depleted and strongly downward-curved (-ve lambda 1 and  
 311 2, respectively) REE abundance patterns compared with MORB and other global ocean floor  
 312 basalts, reflecting their derivation from a prior melt-depleted, spinel peridotite mantle source  
 313 that was even more refractory than that tapped during the genesis of the vast majority of MORB  
 314 (Fig. 6a). We emphasise the projections of slope and curvature of the chondrite-normalised  
 315 REE abundances shown in Fig. 6 unequivocally reveal that Unit 1 ASB basalts are distinct  
 316 compared with FAB of the Izu-Bonin-Mariana arcs<sup>10, 59, 60</sup> and backarc basin basalts of the  
 317 Philippine Sea Plate. The latter are similarly depleted overall in REE but have less downward  
 318 curvature. Furthermore, the sigmoidal character (lambda 3; upward curvature or flexure at the  
 319 light REE end of otherwise concave-downward-sloping patterns) is also distinct between Unit  
 320 1 basalts of the ASB and FAB: the latter have a lesser degree of flexure (Fig. 6b).



321 **Fig. 6.** Shape coefficients of rare earth element patterns<sup>53</sup> for comparison of Unit 1 ASB basalts with FAB,  
 322 MORB/G, and backarc basin basalts of the Philippine Sea Plate. Data sources for a and b are Unit 1<sup>26</sup>, MORB  
 323 from Gale et al.<sup>28</sup> and Jenner & O'Neill<sup>54</sup>, boninite<sup>55-58</sup>, FAB of Izu-Bonin-Mariana<sup>10, 59, 60</sup> and literature  
 324 cited in<sup>18</sup>. **a** Lambda 2 (curvature) versus lambda 1 (slope). **b** Lambda 3 (sigmoidal character) versus lambda  
 325 2. **c** Lambda 2 versus lambda 1 comparing clinopyroxene from Unit 1 and gabbros at Site 1256<sup>61</sup> with ocean  
 326 floor basalts<sup>28, 54</sup> and Unit 1 bulk rock<sup>26</sup>.

328

329 Unit 1 ASB basalts are also distinctive when compared with the majority of active island  
330 arc basalts and boninites<sup>53</sup>. Most of the former overlap the MORB array in lambda 1 vs lambda  
331 2 space, ranging upward from  $\lambda_1$ ,  $\lambda_2$  of -5 and -40 respectively. Boninites plot in the upper  
332 centre of this type of diagram ( $\lambda_1 \sim 0$ ;  $\lambda_2 > 25$ ), reflecting their chondrite-normalised, concave-  
333 upward dish-shaped patterns<sup>53</sup>.

334 A comparison between the chondrite-normalised REE abundance patterns of the  
335 clinopyroxene in Unit 1 and the host rocks is shown in Fig. 6c. Those of the most primitive  
336 (highest  $100 \cdot \text{Mg}/(\text{Mg} + \Sigma \text{Fe})$ ) subunits occupy the extremes of the respective clinopyroxene-  
337 bulk rock data arrays in negative lambda 1 vs 2 space. Fractional crystallisation of  
338 clinopyroxene drives the residual melt towards slightly more positive lambda values along the  
339 ocean floor basalt data array<sup>53</sup>.

340

## 341 **Discussion**

### 342 **Conditions at subduction inception**

343 The petrology and geochemical composition of Unit 1 ASB basalts provides an opportunity to  
344 probe the character of the source mantle extant at subduction inception, and what role the newly  
345 subducting Pacific Plate might have contributed to the earliest magma genesis. Compared with  
346 MORB and backarc basin basalt of the Philippine Sea, Unit 1 ASB basalts have high Mg/Fe,  
347 high Sc, low Ti, Zr, Ti/V, and Zr/Y<sup>22</sup>. They also have globally extreme, chondrite-normalised,  
348 depleted light REE abundance patterns<sup>26</sup> (Fig. 6). The mineralogy of Unit 1 ASB basalts is also  
349 distinctive. A crystallisation sequence of spinel > olivine > plagioclase > clinopyroxene is  
350 inferred, similar to that of MORB. However, the high Mg number and strongly aluminous  
351 character of the clinopyroxene, and persistence until eruption of this phase coupled with the  
352 presence of spinel spanning a large Cr-Al-Fe compositional range, have not previously been  
353 identified in any ocean floor basalt.

354 Collectively, this evidence points to a refractory, albeit clinopyroxene-bearing, upper mantle  
355 source of Unit 1 ASB basalt, that had experienced a larger degree of prior melt extraction than  
356 that tapped during MORB generation<sup>26, 54</sup>. The dry solidus temperature of this type of peridotite  
357 would be higher than that tapped during MORB generation. Partial melting below the ASB  
358 nevertheless occurred ~3 million years after subduction inception, and was in the spinel  
359 peridotite stability field. Contemporaneous tholeiitic basalts preceding boninites were being  
360 erupted in the Mariana forearc<sup>62</sup>. The presence of low-Fe<sup>3+</sup>, Cr-Al-rich spinel is a primary  
361 indicator of reduced conditions during source partial melting (Fig. 4). Given the compositional  
362 zonation of the crystalline phases, and the uncertainty of establishing equilibrium associations,  
363 detailed thermobarometry (via relevant equilibria such as  $2\text{Mg}_2\text{SiO}_4 + \text{CaAl}_2\text{Si}_2\text{O}_8 = \text{MgAl}_2\text{O}_4$   
364  $+ \text{CaMgSi}_2\text{O}_6 + \text{Mg}_2\text{Si}_2\text{O}_6$ ) is not feasible. However, some constraints can be established. If a  
365 range of primary MgO contents in Unit 1 ASB basalts from 12 to 13.5 wt% is correct, then a 1  
366 bar potential temperature ( $T_p$ ) of 1350 to 1400°C is calculated for dry conditions<sup>63</sup>, similar to  
367 temperatures calculated for FAB generation by previous authors<sup>60</sup>. Several lines of evidence  
368 suggest Unit 1 ASB basalts contained dissolved H<sub>2</sub>O in excess of that typical of MORB, that  
369 would reduce these temperatures by ~40°C for ~ 0.5 wt% dissolved H<sub>2</sub>O and be similar to the  
370  $T_p$  of Mg-rich MORB<sup>64</sup>: 1. steepening of the clinopyroxene-in curve by dissolved H<sub>2</sub>O is a  
371 possible explanation for the preservation until eruption of this phase; 2. The high Mg number  
372 of the clinopyroxene is consistent with derivation of the parental Unit 1 ASB basalts directly  
373 from pressures (e.g., ~ 1 GPa) close to the transition from plagioclase- to spinel peridotite facies,  
374 where the difference in temperature of saturation between olivine and clinopyroxene is smaller  
375 than at lower pressures<sup>49</sup>; 3. contrasted degrees of crystallinity and variably anorthitic  
376 plagioclase is consistent with variable amounts of dissolved H<sub>2</sub>O; 3. A pressure-dependent  
377 upper limit (e.g., 2 wt% at 0.5 GPa) to dissolved H<sub>2</sub>O content is established by the persistence  
378 of saturation with plagioclase prior to clinopyroxene<sup>49, 64</sup>. Elevated Rb and U relative to Ba and

379 Th might be an intrinsic feature of unaltered Unit 1 ASB basalts; possibly Rb and U were  
380 introduced by dehydration at shallow (~30 km) depths of the newly descending Pacific Plate  
381 into the proto-mantle wedge of the Izu-Bonin-Mariana arc, that was still hot at shallow depths  
382 through involvement a few million years previously in the production of MORB along the  
383 Izanagi-Pacific Ridge<sup>5</sup>. Retention of Ba and Th in hydrous phases stable at relatively low  
384 pressures (e.g., mica, epidote, monazite) could account for the decoupling of these elements  
385 from Rb and U<sup>65, 66</sup>.

386

### 387 **Arc inception and inheritance**

388 Geochemical and mineralogical differences between the low-Ti-K tholeiitic basalt of the ASB  
389 and FAB may relate to the spatial and temporal evolution of the IBM system during the early  
390 stages of its development. The lower Ti/V of FAB<sup>10, 14, 18, 22</sup> might have resulted from the  
391 tapping of a similarly depleted peridotite source but with an oxidised overprint compared with  
392 that tapped during the generation of basalts in the ASB. For example, V is more incompatible  
393 in olivine-pyroxene-spinel assemblages at higher valence states. Consequently, Ti/V is a  
394 function of prior melt extraction, redox state during various melting episodes, and  
395 pressure/temperature of melting which is also related to H<sub>2</sub>O contents of the source peridotite<sup>67</sup>,  
396 <sup>68</sup>.

397 The REE abundance patterns are not consistent with a more depleted source for FAB  
398 unless a light REE-bearing, subducted slab-derived component was added to the FAB source  
399 and not to the source of ASB basalts. The FAB are also generally less Mg-rich than Unit 1 ASB  
400 basalts, and the high-Mg, aluminous clinopyroxene plus Cr-Al-rich spinel assemblage  
401 characteristic of Unit 1 ASB basalt has not been observed in FAB. Eruption of the relatively  
402 unfractionated Unit 1 basalt requires rapid transit from the wedge sources without the prolonged  
403 staging characteristic of MOR systems<sup>28, 31</sup>. An extensive rifting system within the overriding

404 Philippine Sea Plate, both along- and across-strike of the nascent IBM subduction system is  
405 required, possibly due to rapid slab roll-back<sup>7, 69</sup>. The transition to boninite magma generation  
406 required further partial melting of highly depleted mantle wedge sources but with a greater  
407 imprint of a slab-derived flux both of H<sub>2</sub>O and fluid-mobile trace elements<sup>13, 18</sup>. The melt-  
408 depleted composition of this mantle wedge would have initially formed the sources tapped  
409 during the development of the KPR chain of stratovolcanoes, as sampled by Unit III  
410 pyroclastics<sup>35</sup>.

411

## 412 **Methods**

413 **Scanning electron microscopy.** Scanning electron microscopy in back-scattered electron  
414 imaging mode was used to characterize the morphology of the spinel in thin sections. Analysis  
415 were carried out at the Key Laboratory of Submarine Geosciences, State Oceanic  
416 Administration in China, using a JEOL 8100 probe, with an accelerating voltage of 15 kV,  
417 current of 10 nA and beam spot diameter of 1 μm. Samples were coated with carbon prior to  
418 analysis.

419 **Electron probe micro-analysis.** In situ major elements compositions of minerals were  
420 obtained, both, using a Cameca SX-100 electron probe with 4 spectrometer at the Research  
421 School of Earth Sciences (RSES) in Australian National University (ANU), Canberra,  
422 Australian, and using JEOL-8200 electron probe at Guangzhou Institute of Geochemistry (GIG),  
423 Chinese Academy of Sciences (CAS). The operating conditions were: 15kV of accelerating  
424 voltage, 20 nA of probe current, and 1 μm of the diameter of the electron beam. The counting  
425 times at the peaks were 10s for Si, 20s for Al and Mg, 30s for Ti, Ca, Na and K, 40s for Fe and  
426 Mn, and 60s for Cr and P. Na, Mg, Al, Si and P were determined using K $\alpha$  line obtained with  
427 a TAP crystal, then PET crystal for K, Ca, and Na, and LLIF crystal for Ni, Fe, Mn and Cr.  
428 Natural minerals were used as standards, and all data were corrected with a ZAF program.

429 **Laser ablation inductively coupled plasma-mass spectrometry (LA-ICPMS).** In situ trace  
430 element analyses of minerals were performed both at RSES in ANU, using Coherent  
431 CompexPro 110 laser ablation system connected to an Agilent 7700 ICP-MS, and at GIGCAS  
432 using a Resonetic Resolution S-155 laser ablation system connected on an Agilent 7900 ICP-  
433 MS. The laser spot size was set to 37  $\mu\text{m}$  at ANU and 40  $\mu\text{m}$  at GIGCAS. The analyzing were  
434 operated at constant laser energy of 80 mJ, repetition rate of 6Hz. The ablation time was 40s  
435 with 30s pre-ablation time and 20s post-ablation time. NIST glass 612 was used as a standard  
436 and BCR-2G was used as monitoring standard. The calculations of mineral trace elements  
437 concentrations were performed by ICPMSDataCal 10.8<sup>70</sup>, using <sup>43</sup>Ca as internal standard.

438

439 **Acknowledgments** Our research is based on samples and data initially provided by the  
440 International Ocean Discovery Program. We thank the JOIDES Resolution crew, IODP staff  
441 and shipboard scientific colleagues for their sustained efforts in accomplishing all of the  
442 primary goals of Expedition 351. HL and WS acknowledge funding from XDB42020203 and  
443 the National Natural Science Foundation of China (No. 91328204, 41473029). Funding was  
444 provided by the Australian Research Council via ANZIC through a grant to RJA.

445

446 **Author Contributions:** The first 10 co-authors were participants on International Ocean  
447 Discovery Program Expedition 351, and contributed to establishing the initial lithologic  
448 framework for the research described herein, descriptions of the rock samples and  
449 identification, and discussions. HL obtained the major and trace elements of the mineral  
450 phases via microprobe and laser ablation analysis, photomicrographs, and drafted all figures.  
451 RJA and HL wrote the majority of the paper with inputs from all co-authors.

452

453 The authors declare no conflict of interest.

454

455 **References**

- 456 1. England P., Engdahl R., Thatcher W. Systematic variation in the depths of slabs  
457 beneath arc volcanoes. *Geophysical Journal International* **156**, 377-408 (2004).  
458
- 459 2. Syracuse E. M., Abers G. A. Global compilation of variations in slab depth beneath  
460 arc volcanoes and implications. *Geochemistry Geophysics Geosystems* **7**,  
461 2005GC001045 (2006).  
462
- 463 3. Schmidt M. W. Melting of pelitic sediments at subarc depths: 2. Melt chemistry,  
464 viscosities and a parameterization of melt composition. *Chemical Geology* **404**,  
465 168-182 (2015).  
466
- 467 4. Turner S. J., Langmuir C. H., Katz R. F., Dungan M. A., Escrig S. Parental arc magma  
468 compositions dominantly controlled by mantle-wedge thermal structure. *Nature*  
469 *Geoscience* **9**, 772-776 (2016).  
470
- 471 5. Seton M., Flament N., Whittaker J., Mueller R. D., Gurnis M., Bower D. J. Ridge  
472 subduction sparked reorganization of the Pacific plate-mantle system 60-50  
473 million years ago. *Geophysical Research Letters* **42**, 1732-1740 (2015).  
474
- 475 6. Sun W., Zhang L., Liao R., Sun S., Li C., Liu H. Plate convergence in the Indo-Pacific  
476 region. *Journal of Oceanology and Limnology* doi: **10.1007/s00343-020-0146-y**,  
477 (2020).  
478
- 479 7. Stern R. J. Subduction initiation: spontaneous and induced. *Earth and Planetary*  
480 *Science Letters* **226**, 275-292 (2004).  
481
- 482 8. Gurnis M., *et al.* Incipient subduction at the contact with stretched continental  
483 crust: The Puysegur Trench. *Earth and Planetary Science Letters* **520**, 212-219  
484 (2019).  
485
- 486 9. Cramer F. *et al.* A transdisciplinary and community-driven database to unravel  
487 subduction initiation. *Nature Communications*. doi: **10.1038/s41467-020-**  
488 **17522-9**, (2020).  
489
- 490 10. Reagan M. K., *et al.* Fore-arc basalts and subduction initiation in the Izu-Bonin-  
491 Mariana system. *Geochemistry Geophysics Geosystems* **11**, 2009GC002871 (2010).  
492
- 493 11. Maunder B., Prytulak J., Goes S., Reagan M. Rapid subduction initiation and  
494 magmatism in the Western Pacific driven by internal vertical forces. *Nat Commun*  
495 **11**, 1874 (2020).  
496
- 497 12. Whattam S. A., Stern R. J. Late Cretaceous plume-induced subduction initiation  
498 along the southern margin of the Caribbean and NW South America: The first  
499 documented example with implications for the onset of plate tectonics.  
500 *Gondwana Research* **27**, 38-63 (2015).  
501

- 502 13. Pearce J. A., *et al.* Boninite and harzburgite from leg 125 (Bonin-Mariana forearc):  
503 A case study of magma genesis during the initial stages of subduction.  
504 *Proceedings of the Ocean Drilling Program, Scientific Results* **125**, 623-659 (1992).  
505
- 506 14. Reagan M. K., *et al.* Subduction initiation and ophiolite crust: new insights from  
507 IODP drilling. *International Geology Review* **59**, 1439-1450 (2017).  
508
- 509 15. Falloon TJ and Danyushevsky LV (2000) Melting of refractory mantle at 1.5, 2.0  
510 and 2.5 GPa under anhydrous and H<sub>2</sub>O-undersaturated conditions: implications for  
511 the petrogenesis of high-Ca boninites and the influence of subduction components  
512 on mantle melting. *Journal of Petrology* **41**: 147-283.
- 513 16. Ishizuka, O., Kimura, J.-I., Li, Y. B., Stern, R. J., Reagan, M. K., Taylor, R. N., Ohara, Y.,  
514 Bloomer, S. H., Ishii, T. & Hargrove, U. S. Early stages in the evolution of Izu–Bonin  
515 arc volcanism: New age, chemical, and isotopic constraints. *Earth and Planetary*  
516 *Science Letters* **250**, 385-401 (2006).  
517
- 518 17. Ishizuka, O., Tani, K., Reagan, M. K., Kanayama, K., Umino, S., Harigane, Y.,  
519 Sakamoto, I., Miyajima, Y., Yuasa, M. & Dunkley, D. J. The timescales of subduction  
520 initiation and subsequent evolution of an oceanic island arc. *Earth and Planetary*  
521 *Science Letters* **306**, 229-240 (2011).  
522
- 523 18. Reagan M. K., Heaton D. E., Schmitz M. D., Pearce J. A., Shervais J. W., Koppers A. A.  
524 P. Forearc ages reveal extensive short-lived and rapid seafloor spreading following  
525 subduction initiation. *Earth and Planetary Science Letters* **506**, 520-529 (2019).
- 526 19. Kanayama, K., Umino, S. & Ishizuka, O. Eocene volcanism during the incipient stage  
527 of Izu–Ogasawara Arc: Geology and petrology of the Mukojima Island Group, the  
528 Ogasawara Islands. *Island Arc* **21**, 288-316, (2012).  
529
- 530 20. Ishizuka, O., Taylor, R.N., Umino, S. & Kanayama, K. Geochemical evolution of arc  
531 and slab following subduction initiation: a record from the Bonin islands, Japan.  
532 *Journal of Petrology*, ega050 *in press*. (2020).  
533
- 534 21. Brounce M., Kelley K. A., Cottrell E., Reagan M. K. Temporal evolution of mantle  
535 wedge oxygen fugacity during subduction initiation. *Geology* **43**, 775-778 (2015).  
536
- 537 22. Arculus R. J., *et al.* A record of spontaneous subduction initiation in the Izu-Bonin-  
538 Mariana arc. *Nature Geoscience* **8**, 728-733 (2015).  
539
- 540 23. Ishizuka O., *et al.* Age of Izu-Bonin-Mariana arc basement. *Earth and Planetary*  
541 *Science Letters* **481**, 80-90 (2018).  
542
- 543 24. Lallemand, S. Philippine Sea plate inception, evolution, and consumption with special  
544 emphasis on the early stages of Izu-Bonin-Mariana subduction. *Progress in Earth and*  
545 *Planetary Science* **3**, doi: 10.1186/s40645-016-0085-6, (2016).  
546
- 547 25. Ryan W. B. F., *et al.* Global Multi-Resolution Topography synthesis. *Geochemistry*  
548 *Geophysics Geosystems* **10**, (2009).  
549

- 550 26. Hickey-Vargas R., *et al.* Origin of depleted basalts during subduction initiation  
551 and early development of the Izu-Bonin-Mariana island arc: Evidence from IODP  
552 expedition 351 site U1438, Amami-Sankaku basin. *Geochimica Et Cosmochimica*  
553 *Acta* **229**, 85-111 (2018).  
554
- 555 27. Arculus R. J., Ishizuka O., Bogus K., scientists E. Expedition 351 summary. In  
556 Arculus, R.J., Ishizuka, O. & Bogus, K. (eds) Proc. Int. Ocean Disc. Prog., 351.  
557 (2015).  
558
- 559 28. Gale A., Dalton C. A., Langmuir C. H., Su Y., Schilling J.-G. The mean composition of  
560 ocean ridge basalts. *Geochemistry Geophysics Geosystems* **14**, 489-518 (2013).  
561
- 562 29. Lebas M. J., Lemaitre R. W., Streckeisen A., Zanettin B. A Chemical Classification of  
563 Volcanic Rocks Based on the Total Alkali-Silica Diagram. *Journal of Petrology* **27**,  
564 745-750 (1986).  
565
- 566 30. Francis D. The pyroxene paradox in MORB glasses - A signature of picritic  
567 parental magmas ? . *Nature* **319**, 586-589 (1986).  
568
- 569 31. O'Neill H. S. C., Jenner F. E. The global pattern of trace-element distributions in  
570 ocean floor basalts. *Nature* **491**, 698-705 (2012).  
571
- 572 32. Dick H. *et al.* Lithostratigraphic evolution of an in situ section of oceanic layer 3.  
573 *Proc Ocean Drilling Program, Scientific Results* **118**, 439-515 (1991).  
574
- 575 33. Morimoto N., *et al.* Nomenclature of pyroxenes. *American Mineralogist* **73**, 1123-  
576 1133 (1988).  
577
- 578 34. Waldman R. J., *et al.* Sedimentary and Volcanic Record of the Nascent IBM Arc  
579 from IODP Site U1438. *Geological Society of America inpress*, (2020).  
580
- 581 35. Brandl P. A., *et al.* The arc arises: The links between volcanic output, arc evolution  
582 and melt composition. *Earth and Planetary Science Letters* **461**, 73-84 (2017).  
583
- 584 36. Whattam S. A., *et al.* Mineral compositions and thermobarometry of basalts and  
585 boninites recovered during IODP Expedition 352 to the Bonin forearc. *American*  
586 *Mineralogist in press*, (2020).  
587
- 588 37. Alabaster T., Pearce J. A., Malpas J. The volcanic stratigraphy and petrogenesis of  
589 the Oman Ophiolite complex. *Contributions to Mineralogy and Petrology* **81**, 18-  
590 183 (1982).  
591
- 592 38. Barnes S. J., Roeder P. L. The range of spinel compositions in terrestrial mafic and  
593 ultramafic rocks. *Journal of Petrology* **42**, 2279-2302 (2001).  
594
- 595 39. Kamenetsky V. S., Crawford A. J., Meffre S. Factors controlling chemistry of  
596 magmatic spinel: An empirical study of associated olivine, Cr-spinel and melt  
597 inclusions from primitive rocks. *Journal of Petrology* **42**, 655-671 (2001).  
598

- 599 40. Sigurdsson H., Schilling J. G. Spinels in Mid-Atlantic Ridge basalts: Chemistry and  
600 occurrence. *Earth and Planetary Science Letters* **29**, 7-20 (1976).  
601
- 602 41. Warren J. M. Global variations in abyssal peridotite compositions. *Lithos* **248**,  
603 193-219 (2016).  
604
- 605 42. Irvine, T.N. Chromian spinel as a petrogenetic indicator Part1. Theory. *Canadian*  
606 *Journal of Earth Sciences* **2**, 648-672 (1965).  
607
- 608 43. Meyer P. S., Dick H. J. B., Thompson G. Cumulate gabbros from the Southwest  
609 Indian Ridge, 54° S-7° 16' E: implications for magmatic processes at a slow  
610 spreading ridge. *Contributions to Mineralogy and Petrology* **103**, 44-63 (1989).  
611
- 612 44. Arculus R. J., Wills K. J. A. The petrology of plutonic blocks and inclusions from the  
613 Lesser Antilles island arc. *Journal of Petrology* **21**, 743-799 (1980).  
614
- 615 45. Melekhova E., Blundy J., Martin R., Arculus R., Pichavant M. Petrological and  
616 experimental evidence for differentiation of water-rich magmas beneath St. Kitts,  
617 Lesser Antilles. *Contributions to Mineralogy and Petrology* **172**, (2017).  
618
- 619 46. Wood B. J., Blundy J. D. *Trace element partitioning: the influences of ionic radius,*  
620 *cation charge, pressure, and temperature* (2014).  
621
- 622 47. Sun S. S., McDonough W. F. Chemical and isotopic systematics of oceanic basalts:  
623 Implications for mantle composition and processes. In *Saunders, AD, & Norry, MJ*  
624 *(eds) Magmatism in the Ocean Basins, Geological Society London Special*  
625 *Publications* **42**, 313-345 (1989).  
626
- 627 48. O'Neill H. S. C., Jenner F. E. Causes of the Compositional Variability among Ocean  
628 Floor Basalts. *Journal of Petrology* **57**, 2163-2193 (2016).  
629
- 630 49. Feig S. T., Koepke J., Snow J. E. Effect of water on tholeiitic basalt phase equilibria:  
631 an experimental study under oxidizing conditions. *Contributions to Mineralogy*  
632 *and Petrology* **152**, 611-638 (2006).  
633
- 634 50. Hofmann A. W., Jochum K. P., Seufert M., White W. M. Nb and Pb in oceanic  
635 basalts: new constraints on mantle evolution. *Earth and Planetary Science Letters*  
636 **79**, 33-45 (1986).  
637
- 638 51. Kelley K. A., Plank T., Ludden J., Staudigel H. Composition of altered oceanic crust  
639 at ODP Sites 801 and 1149. *Geochemistry Geophysics Geosystems* **4**, (2003).  
640
- 641 52. Yogodzinski G. M., *et al.* Implications of Eocene-age Philippine Sea and forearc  
642 basalts for initiation and early history of the Izu-Bonin-Mariana arc. *Geochimica*  
643 *Et Cosmochimica Acta* **228**, 136-156 (2018).  
644
- 645 53. O'Neill H. S. C. The Smoothness and Shapes of Chondrite-normalized Rare Earth  
646 Element Patterns in Basalts. *Journal of Petrology* **57**, 1463-1508 (2016).  
647

- 648 54. Jenner F. E., O'Neill H. S. C. Analysis of 60 elements in 616 ocean floor basaltic  
649 glasses. *Geochemistry Geophysics Geosystems* **13**, 2011GC004009 (2012).  
650
- 651 55. Coulthard Jr. D. A. Subduction initiation and igneous petrogenesis: characterizing  
652 melt generation at a new convergent boundary through the geochemical analysis  
653 of volcanic glass. *MS thesis, University of Iowa*, <https://ir.uiowa.edu/etd/6398>  
654 (2018).  
655
- 656 56. Kanayama K., Umino S., Ishizuka O. Eocene volcanism during the incipient stage  
657 of Izu-Ogasawara Arc: Geology and petrology of the Mukojima Island Group, the  
658 Ogasawara Islands. *Island Arc* **21**, 288-316 (2012).  
659
- 660 57. Umino S., *et al.* Did boninite originate from the heterogeneous mantle with  
661 recycled ancient slab? *Island Arc* **27**, e12221 (2018).  
662
- 663 58. Valetich M. J., Mavrogenes J., Arculus R., Umino S. Evolution of chalcophile  
664 elements in the magmas of the Bonin Islands. *Chemical Geology* **508**, 234-249  
665 (2019).  
666
- 667 59. Li H.-Y., *et al.* Radiogenic isotopes document the start of subduction in the  
668 Western Pacific. *Earth and Planetary Science Letters* **518**, 197-210 (2019).  
669
- 670 60. Shervais J. W., *et al.* Magmatic Response to Subduction Initiation: Part 1. Fore-arc  
671 Basalts of the Izu-Bonin Arc From IODP Expedition 352. *Geochemistry Geophysics*  
672 *Geosystems* **20**, 314-338 (2019).  
673
- 674 61. Koepke J., *et al.* Gabbros from IODP Site 1256, equatorial Pacific: Insight into axial  
675 magma chamber processes at fast spreading ocean ridges. *Geochemistry*  
676 *Geophysics Geosystems* **12**, 2011GC003655 (2011).  
677
- 678 62. Cosca, M.A., Arculus, R.J., Pearce, J.A., Mitchell, J.G. 40Ar/39Ar and K-Ar  
679 geochronological age constraints for the inception and early evolution of the Izu-  
680 Bonin-Mariana arc system. *The Island Arc* **7**, 579-595 (1998).  
681  
682
- 683 63. Herzberg C., Asimow P. D. PRIMELT3 MEGA.XLSM software for primary magma  
684 calculation: Peridotite primary magma MgO contents from the liquidus to the  
685 solidus. *Geochemistry Geophysics Geosystems* **16**, 563-578 (2015).  
686
- 687 64. Medard E., Grove T. L. The effect of H<sub>2</sub>O on the olivine liquidus of basaltic melts:  
688 experiments and thermodynamic models. *Contributions to Mineralogy and*  
689 *Petrology* **155**, 417-432 (2008).  
690
- 691 65. Arculus R. J., Lapierre H., Jaillard E. Geochemical window into subduction and  
692 accretion processes: Raspas metamorphic complex, Ecuador. *Geology* **27**, 547-  
693 550 (1999).  
694
- 695 66. Spandler C., Hermann J., Arculus R., Mavrogenes J. Redistribution of trace  
696 elements during prograde metamorphism from lawsonite blueschist to eclogite

697 facies; implications for deep subduction-zone processes. *Contributions to*  
698 *Mineralogy and Petrology* **146**, 205-222 (2003).  
699  
700 67 Mallmann, G., O'Neill, H.StC. Ther c rystal/melt partitioning of V during mantle  
701 melting as a funcgtion of oxygen fugacity compared with some other elements  
702 (Al, P, Ca, Sc, Ti, Cr, Fe, Ga, Y, Zr and Nb. *Journal of Petrology* **50**, 1765-1794  
703 (2009).  
704  
705 68 Wang, J., Xiong, X., Takahashi, E., Zhang, L., Li, L., Liu, X. Oxidation state of arc  
706 mantle revealed by partitioning of V, Sc, and Ti betyween mantle minerals and  
707 basaltic melts. *Journal of Geophysical Research: Solid Earth* **124**, 4617-4638  
708 (2019).  
709  
710 69. Stern R. J. Subduction zones. *Reviews of Geophysics* **40**, (2002).  
711  
712 70. Liu Y. S., *et al.* In situ analysis of major and trace elements of anhydrous minerals  
713 by LA-ICP-MS without applying an internal standard. *Chemical Geology* **257**, 34-  
714 43 (2008).  
715

716

717 **Supplementary Tables**

718 Supplementary 1 Table 1. Major and trace element compositions for clinopyroxene in Unit 1  
719 ASB basalt.

720 Supplementary 1 Table 2. Major element compositions of clinopyroxene in Unit 1 ASB  
721 basalt.

722 Supplementary 1 Table 3. Major elements compositions of clinopyroxene in Unit 3.

723 Supplementary 1 Table 4. Major element compositions of spinel in Unit 1 ASB basalt. (ND =  
724 not detected)

725 Supplementary 1 Table 5. Major element compositions of plagioclase in Unit 1 ASB basalt.

726 Supplementary 2 Table 1. Summary of replicate analyses of trace element of reference

727 standard BCR-2G compared to the GeoReM preferred values for each element. See

728 <http://georem.mpch-mainz.gwdg.de/> for recommended

# Figures

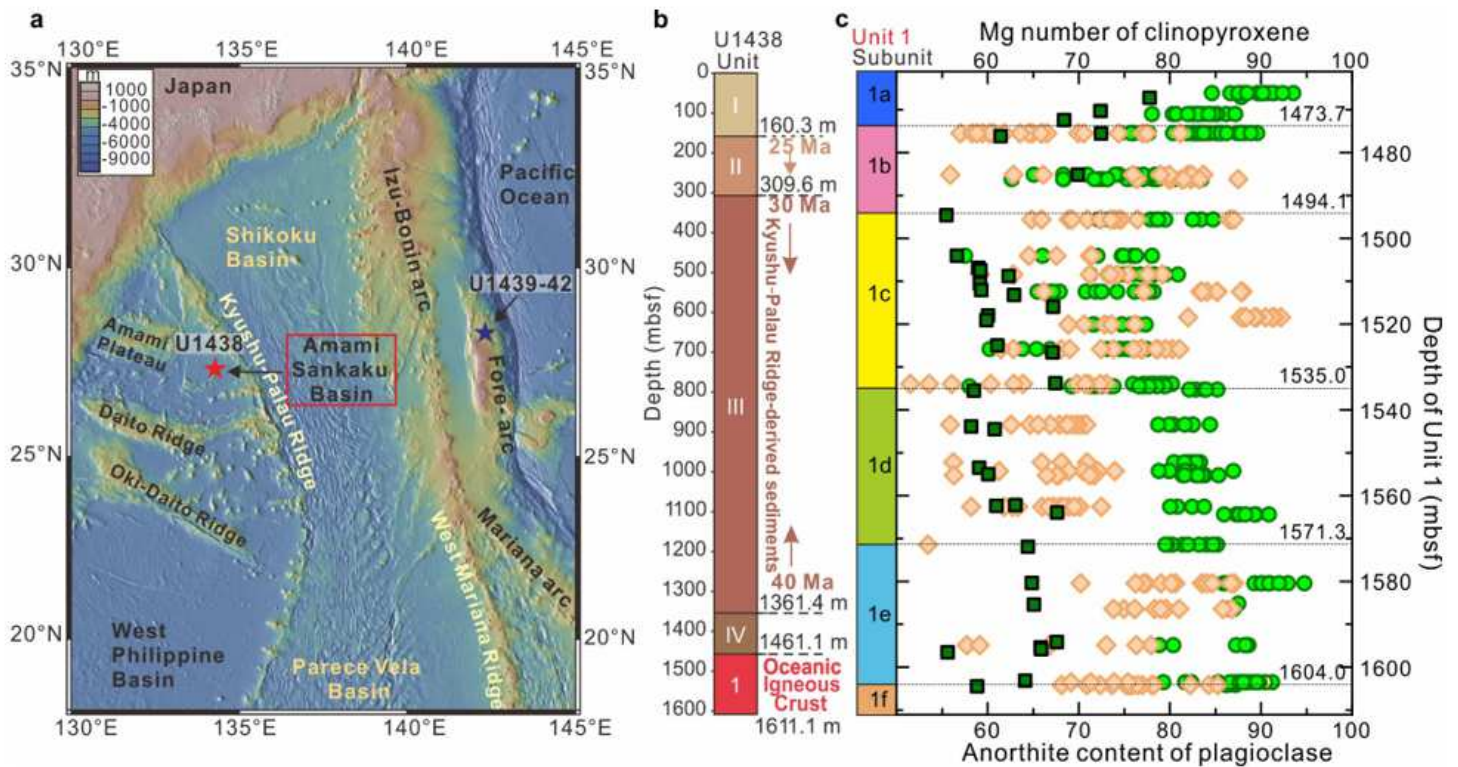


**Figure 1**

Location of IODP expeditions 351 (U1438) and 352 (U1439-42) drill sites, stratigraphy of U1438, bulk rock and mineral characteristics of Unit 1 at Site U1438. a Bathymetric map showing location of Amami-Sankaku Basin and Site U1438 adjacent to the Kyushu-Palau Ridge (remnant arc), and sites U1439-42 (Expedition 352) in the present-day fore-arc. b Unit thicknesses and ages at Site U1438. c subunit information for Unit 1 including Mg number ( $100 \times \text{Mg}/(\text{Mg} + \text{Fe}^{2+})$ ) of clinopyroxene (green circles), anorthite content (An%) of plagioclase (orange diamonds), and bulk rock  $100 \times \text{Mg}/(\text{Mg} + \Sigma\text{Fe})$  (dark green squares) versus depth. Note: The designations employed and the presentation of the material on this map do not imply the expression of any opinion whatsoever on the part of Research Square concerning the legal status of any country, territory, city or area or of its authorities, or concerning the delimitation of its frontiers or boundaries. This map has been provided by the authors.

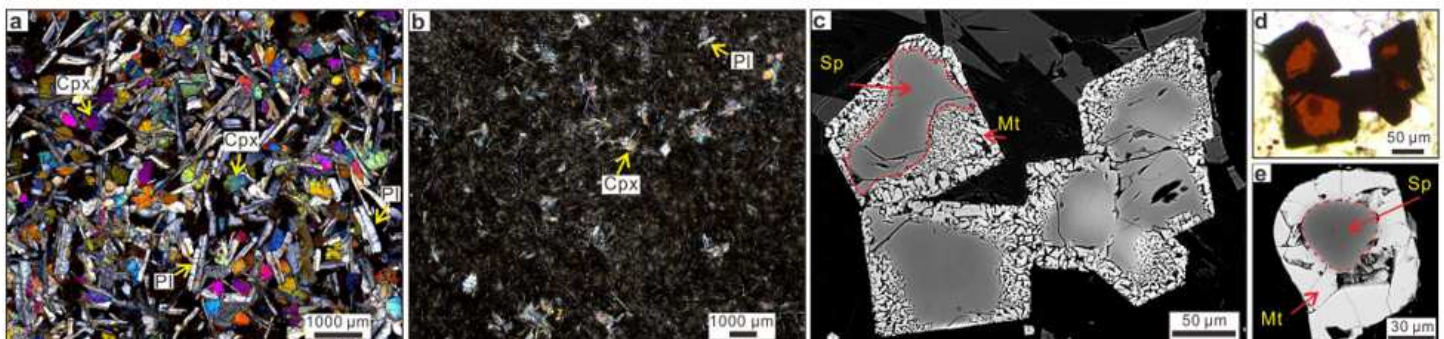


**Figure 2**

General and detailed photomicrographs of Unit 1 ASB basalts. a Medium-grained basalt from subunit 1c (78R3 21-25), including clinopyroxene (Cpx) and plagioclase (Pl) crystals (crossed polars). b Fine-grained basalt (84R1 84-87) from subunit 1e, with small crystals of clinopyroxene and plagioclase (crossed polars). c Back-scatter electron images of spinel; darker color within the red dash line is aluminous spinel; brighter color outside the red dash line is symplectitic magnetite. d Transmitted light image of the same spinel shown in c, red color is the Al-rich cores, and opaque boundaries are magnetite. e Back-scatter image of spinel, Al-rich core surrounded by magnetite-rich rim outside the red dash line.

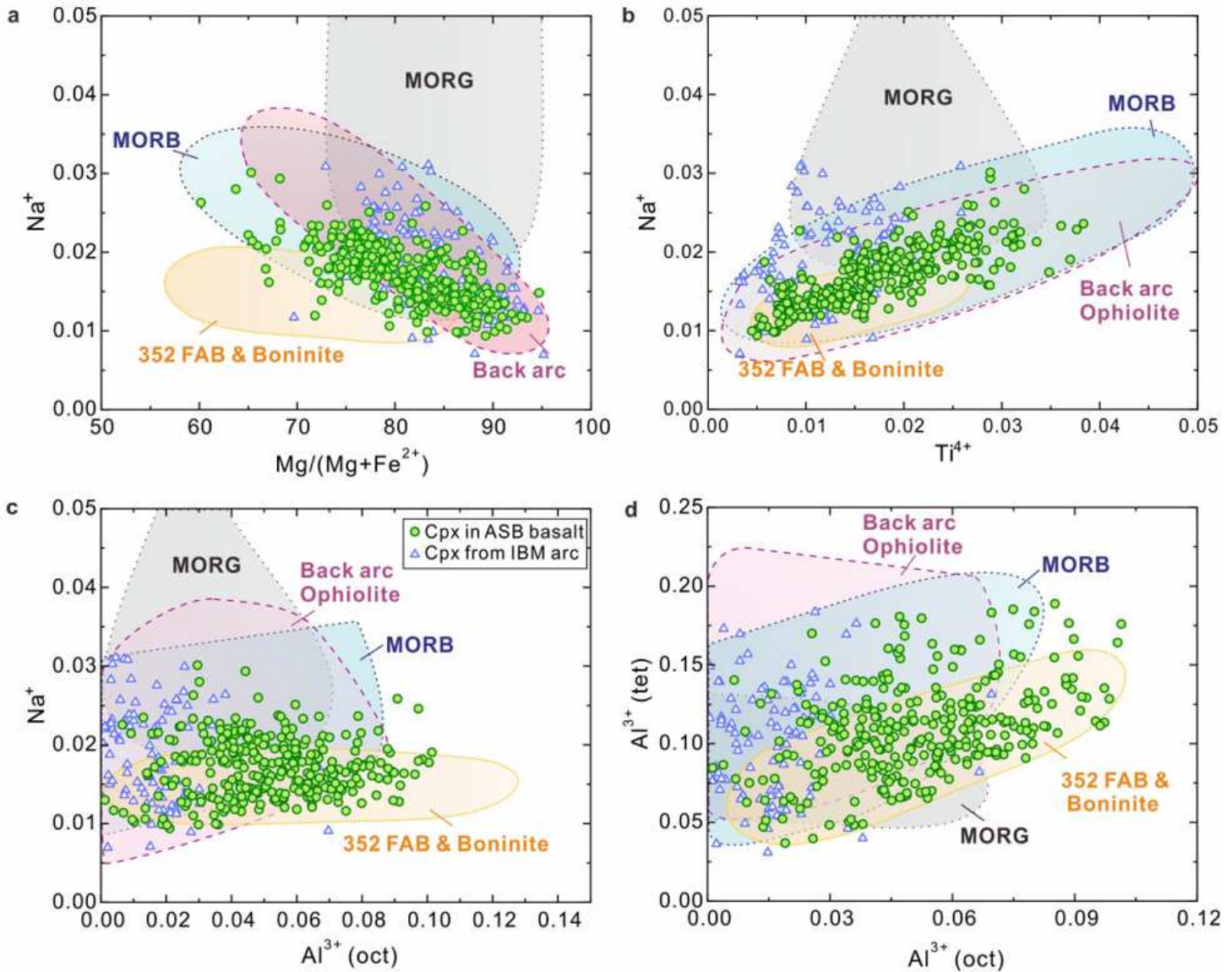


**Figure 3**

Clinopyroxene compositions in 351 Unit 1 of ASB basalt compared with 351 Unit IV recording the nascent IBM arc34 just above the ASB basalt, mid-ocean ridge basalt and gabbro (MORB/G), 352 FAB and boninite36, Oman ophiolite37 and backarcs (Data from PetDatabase website). a  $\text{Na}^+$  versus  $100 \times \text{Mg}/(\text{Mg}+\text{Fe}^{2+})$  for clinopyroxene in Unit 1 ASB basalt and Unit IV recording the nascent IBM arc34,

showing compositional overlap compared with clinopyroxene in MORB/G and backarcs, but a contrasted trend compared with FAB and boninite; b. Na<sup>+</sup> versus Ti<sup>4+</sup>. c Na<sup>+</sup> versus octahedrally-coordinated Al<sup>3+</sup>. d Tetrahedrally-coordinated versus octahedrally-coordinated Al<sup>3+</sup> (Al<sup>3+</sup> (tet) and Al<sup>3+</sup> (oct) respectively). All cations calculated on the basis of 6 oxygen anions. References for data sources used for clinopyroxene in MORB/G are in the Supplementary Material.

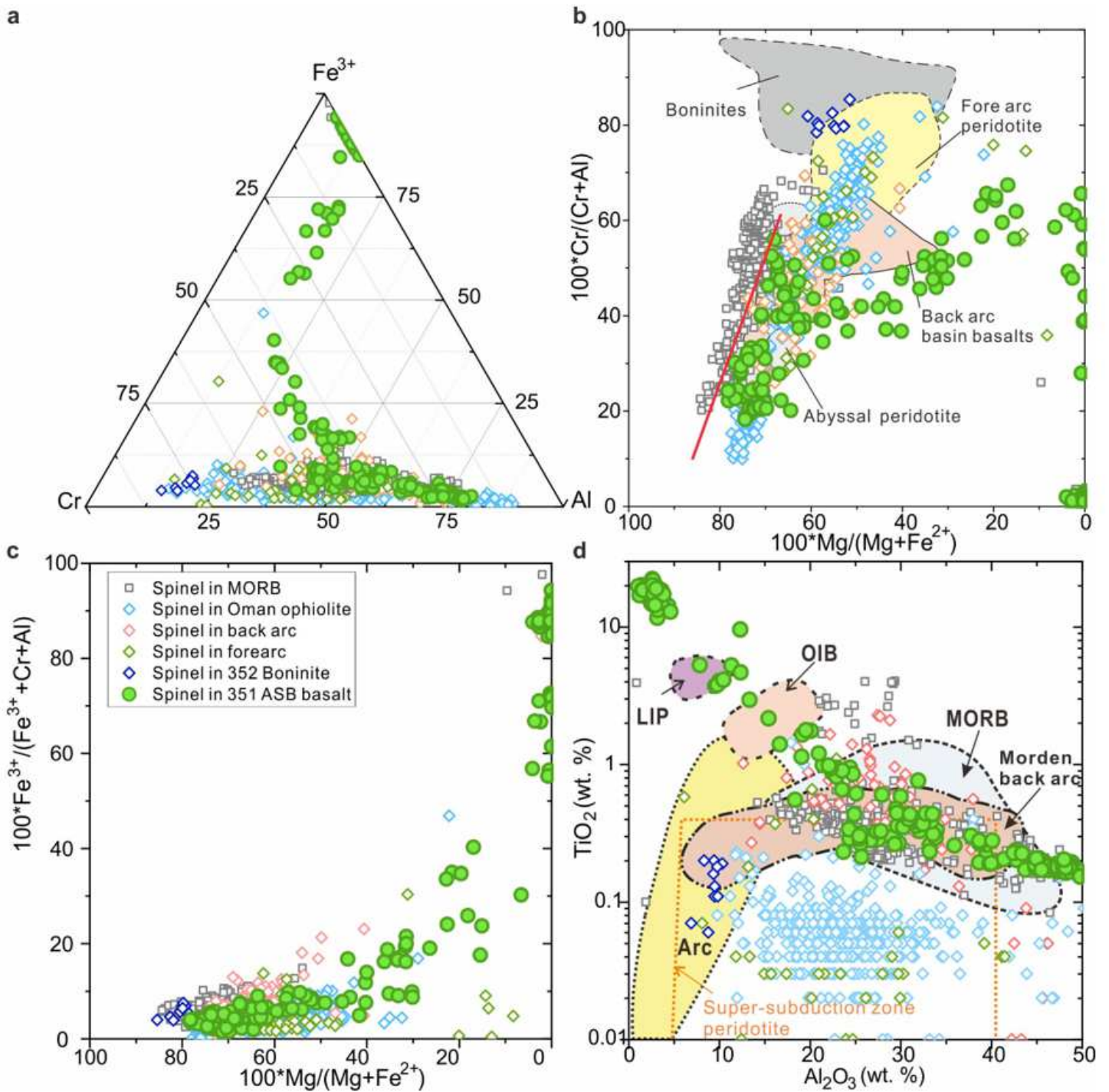


**Figure 4**

Spinel compositions in 351 Unit 1 ASB basalt compared with mid-ocean ridge basalts (MORB) 38, 40, 352 boninite 36, forearc, backarc and Oman ophiolite (data from PetDatabase website) a Cr-Al-Fe<sup>3+</sup> cation

diagram. b  $100 \cdot \text{Cr}/(\text{Cr}+\text{Al})$  versus  $100 \cdot \text{Mg}/(\text{Mg}+\text{Fe}^{2+})$ . c  $100 \cdot \text{Fe}^{3+}/(\text{Fe}^{3+}+\text{Cr}+\text{Al})$  versus  $100 \cdot \text{Mg}/(\text{Mg}+\text{Fe}^{2+})$ . d  $\text{TiO}_2$  (wt. %) versus  $\text{Al}_2\text{O}_3$  (wt.%). Green solid circles are spinel in unit 1 and gray solid square symbols are spinel in MORB. Red line in b delimits the highest  $\text{Mg}/(\text{Mg}+\text{Fe}^{2+})$  for a given  $\text{Cr}/(\text{Cr}+\text{Al})$  of the abyssal harzburgite array<sup>41</sup>. Other abbreviations are: OIB = ocean island basalt; LIP = large igneous province.

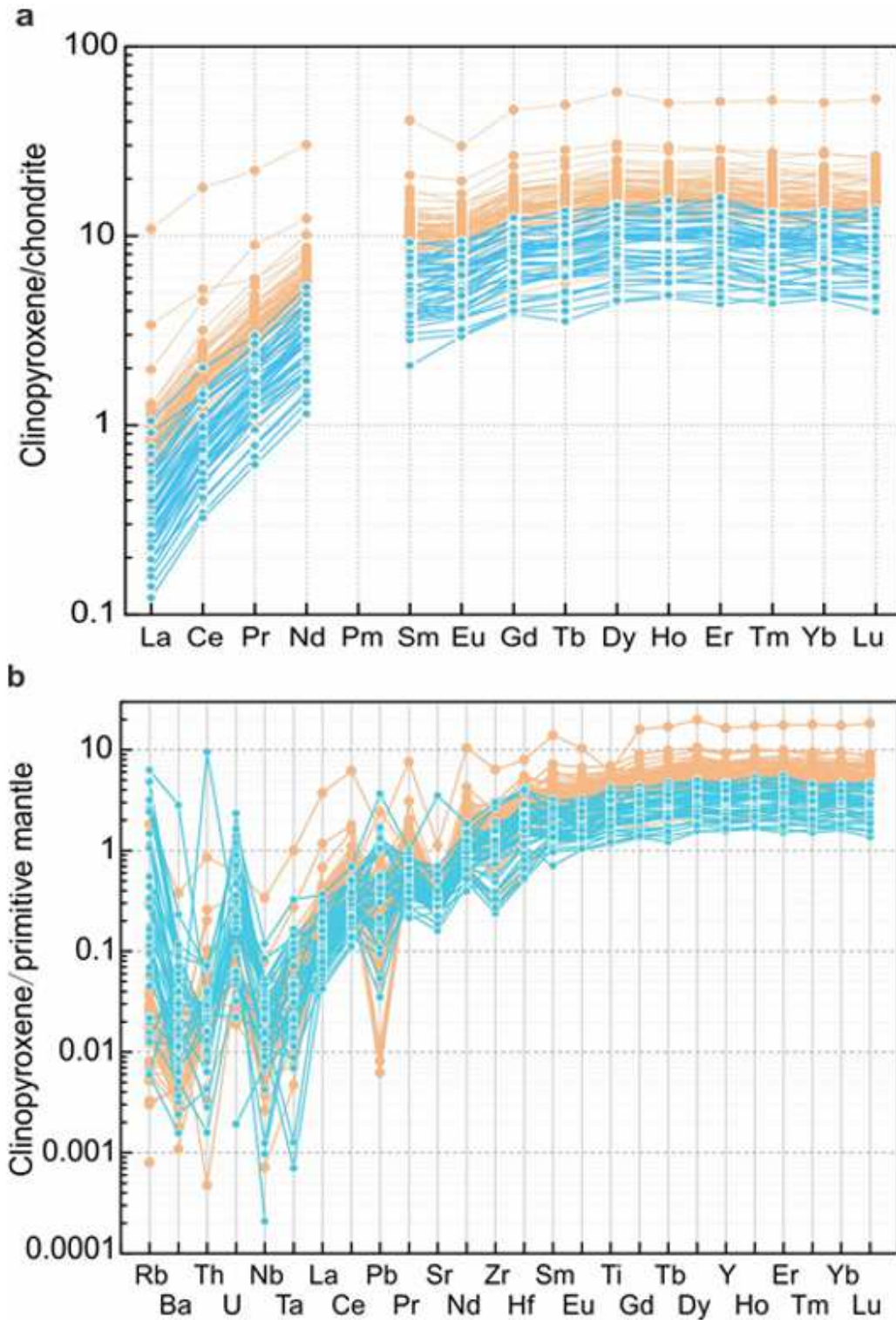
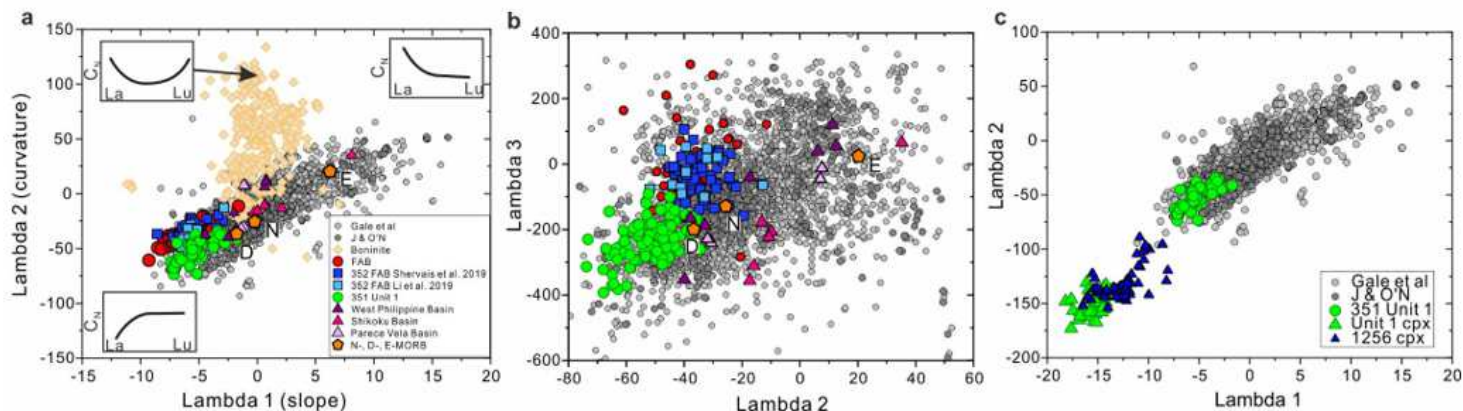


Figure 5

Trace element abundances for clinopyroxene. a Chondrite-normalized<sup>47</sup> rare earth element abundances for clinopyroxene in subunits 1c and 1e of ASB basalts. b Primitive mantle-normalized<sup>47</sup> trace element abundances for clinopyroxene in subunits 1c and 1e. Yellow circles are data for subunit 1c and blue-green circles for subunit 1e.



**Figure 6**

Shape coefficients of rare earth element patterns<sup>53</sup> for comparison of Unit 1 ASB basalts with FAB, MORB/G, and backarc basin basalts of the Philippine Sea Plate. Data sources for a and b are Unit 126, MORB from Gale et al.<sup>28</sup> and Jenner & O'Neill<sup>54</sup>, boninite<sup>55-58</sup>, FAB of Izu-Bonin-Mariana<sup>10, 59, 60</sup> and literature cited in<sup>18</sup>. a Lambda 2 (curvature) versus lambda 1 (slope). b Lambda 3 (sigmoidal character) versus lambda 2. c Lambda 2 versus lambda 1 comparing clinopyroxene from Unit 1 and gabbros at Site 125661 with ocean floor basalts<sup>28, 54</sup> and Unit 1 bulk rock<sup>26</sup>.

## Supplementary Files

This is a list of supplementary files associated with this preprint. Click to download.

- [SupplementaryMaterial.docx](#)
- [S1Table1.xlsx](#)
- [S1Table2.xlsx](#)
- [S1Table3.xlsx](#)
- [S1Table4.xlsx](#)
- [S1Table5.xlsx](#)
- [S2Table1.xlsx](#)